Article:
Nurut Agusutrisno, M., Marrows, C.H. orcid.org/0000-0003-4812-6393, Kamataki, K. orcid.org/0000-0002-3642-4249 et al. (5 more authors) (2023) On-axis Sputtering Fabrication of $Tm_3Fe_5O_{12}$ Film with Perpendicular Magnetic Anisotropy. Thin Solid Films, 788. 140176. ISSN 0040-6090

https://doi.org/10.1016/j.tsf.2023.140176

On-axis Sputtering Fabrication of $Tm_3Fe_5O_{12}$ Film with Perpendicular Magnetic Anisotropy

Marlis Nurut Agusutrisno[a], Christopher H. Marrows[b], Kunihiro Kamataki[c], Takamasa Okumura[c], Naho Itagaki[c], Kazunori Koga[c], Masaharu Shiratani[c], and Naoto Yamashita[b,c*]

[a] Graduate School of Information Science and Electrical Engineering, Kyushu University, Fukuoka, Fukuoka, Japan

[b] School of Physics and Astronomy, University of Leeds, Leeds LS2 9JT, United Kingdom

[c] Faculty of Information Science and Electrical Engineering, Kyushu University, Fukuoka, Fukuoka, Japan

* Corresponding author.

E-mail address: yamashita.naoto.952@m.kyushu-u.ac.jp

Keywords: spintronics, sputtering, Rare-earth iron garnet, Perpendicular magnetic anisotropy

(Dated: 18 October 2023)

ABSTRACT

Thulium iron garnet, $Tm_3Fe_5O_{12}$ with perpendicular magnetic anisotropy is fabricated using an on-axis sputtering technique followed by annealing, whereas previous reports have used unusual off-axis geometries. Stoichiometric $Tm_3Fe_5O_{12}$ is obtained after the modification of the deposition conditions involving the position of the substrate relative to the cathode, which affects both the chemical and structural properties. The effective perpendicular magnetic anisotropy of 8.6 kJ/m^3 is well in line with the results of previous studies using pulse laser deposition and off-axis sputtering. A maze domain pattern is observed, and the domain-wall energy is evaluated as 0.69 mJ/m^2.

1. Introduction

Rare-earth iron garnets have attracted much attention as a materials platform in spintronics because of the rareness of ferrimagnetic insulators, which allow a long-range propagation of spin waves [1–3]. Through the manipulation of the magnetic moment with spin-orbit torque [3], these magnetic insulators are considered as candidates for energy-efficient magnetic memory and logic devices [4]. Furthermore, the low magnetic damping constant of rare-earth iron garnet has the potential to realize the domain-wall qubit [5,6].

For application to integrated systems, perpendicular magnetic anisotropy (PMA) is beneficial, in addition to the weak magnetic moment stemming from the compensated ferrimagnetism [7–11]. Kubota *et. al.* demonstrated a PMA thin film using very thin (46 nm in thickness) thulium iron garnet, $Tm_3Fe_5O_{12}$ (TmIG), on a $Gd_3Ga_5O_{12}$ (GGG) (111) substrate by taking advantage of the large negative magnetostriction constant of λ_{111}= -5.2×10^{-6} and the epitaxial strain of +0.49% [7] followed by the demonstrations of the topological Hall effect [10], spin-orbit torque switching [8], and the creation and transport of skyrmions [11]. Rosenberg *et al* systematically studied the effect of Y-substitution on the magnetic anisotropy [12]. Wu *et. al.* demonstrated the fabrication of TmIG using off-axis sputtering, and showed the saturation magnetization of 99 kA/m, which is close to the bulk value [13]. They also disclosed that the magnetic anisotropy largely depends on the longitudinal distance between the sputtering target and the substrate because of the strain dependence on the chemical composition of the film [14].

The production of TmIG film has been limited to pulsed laser deposition (PLD) [8,12,15] and off-axis sputtering methods [13,14]. Because PLD limits the size of the available wafers, sputtering is more useful for manufacturing. Although off-axis sputtering provides an opportunity to fabricate TmIG by reducing ion bombardment [14,15], the effect of the plasma damage is poorly understood. An important challenge in advancing research in this field is exploring a

simple method to fabricate TmIG films: *on-axis* sputtering, which is usually applied to fabricate oxide thin films on a large scale [16]. Here, we demonstrate the fabrication of TmIG with PMA through on-axis sputtering followed by thermal annealing.

2. Experimental details

2.1 Thin film fabrication

TmIG thin films were grown on GGG (111) substrates through radiofrequency (RF) magnetron sputtering with on-axis geometry. Different substrate positions in the holder and different deposition times were examined. The layout of substrate holder and the sputtering target is shown in Fig. 1a. The distance L between the surface normal of the target and the substrate holder was 55.5 mm, while the angle formed between L and the surface normal of the substrate holder was 20°. A commercially available sputtering target of TmIG, with a diameter of 50.8 mm and a thickness 3 mm (purity of 99.9%, KOJUNDO CHEMICAL LABORATORY), was placed on a magnetron cathode. Three different positions on a sample holder are labelled A, B, and C. A top-view schematic of the sample holder is shown in Fig. 1b. The blue cross indicates the point at which the line extending the center line intersects the substrate holder. The pink squares represent GGG substrates (10 mm × 10 mm) on the sample holder. L_A = 64 mm, L_B = 93 mm, and L_C = 98 mm denote center-to-center distances between the target and each substrate. ϕ_A = 15°, ϕ_B = 36°, and ϕ_C = 39° were the angles formed with respect to the L. The flow rates of oxygen and argon were set as 5 and 18 standard cm^3/min, respectively. The total pressure was kept at 3 Pa during deposition which was performed by supplying RF power of 60 W to the cathode. After the sputtering deposition, post-annealing at 800°C for 3 hours was carried out in an oxygen atmosphere at ambient pressure. Deposition was conducted for 30, 90, 120, and 150 minutes (6, 18, 24, and 30 nm in thick) to confirm that the magnitude of the X-ray diffraction (XRD) peak of

TmIG increased with the thickness.

2.2 Thin film characterization

The structural analysis of TmIG was carried out adopting high-resolution XRD 2θ-ω scan with Cu kα (λ = 1.5406 Å) and X-ray reflectivity (XRR) measurement techniques using a Bruker-D8 Discover. The composition of TmIG was measured adopting the X-ray fluorescence (XRF) (Rigaku Primus II), by utilizing the fundamental parameters calculation method available on the XRF equipment. The magnetic moment was examined using a superconducting quantum interference device (SQUID) (Quantum Design, MPMS3) with DC scan at 300K. The ferromagnetic resonance (FMR) was measured using an electron spin resonance system (Bruker EMX). A piece of substrate was cut into 4 mm × 2 mm in size and pasted on a quartz stick. The frequency of applied microwave was 9.6 GHz, and the power was 2.1 mW. Angle dependence measurements were performed by changing the angle between the external magnetic field and the substrate normal with a DC magnetic field scan at each angle. A Kerr microscope (Evico microscope) was used to visualize the structure of the magnetic domains. A maze domain structure at zero field was examined by an ac demagnetizing procedure [17]. The surface roughness was examined using an atomic force microscope (AFM) (AFM5100N Hitachi).

3. Results and discussion

3.1 Crystal structures

XRD measurements were carried out to confirm the formation of the crystal of TmIG. Figure 2a shows the results of XRD 2θ-ω scans of the samples deposited at position A for different times (30, 90, 150 min) followed by annealing. All the samples showed a peak at 51.55° stemming from TmIG (444) in addition to the peak of substrates at 51.06°. The peak same as that in a

previous study [7] implies that the TmIG film had the same lattice strain as films in the previous study, which is expected to provide PMA. Thus, the feasibility of on-axis sputtering to fabricate TmIG was confirmed by these XRD patterns. Thick films with t = 13, 24, and 30 nm showed that the peak from TmIG(444). The intensity of the TmIG peak increased with the deposition time at on-axis position A.

To check the dependence of the attainability of TmIG on the position, three samples were grown under the same condition with a film thickness of 24 nm and examined as shown in Fig. 2b. Interestingly a clear peak of TmIG(444) only appeared for a sample deposited at position A. In addition, the thickness of the TmIG film t depended on the position, which was measured by XRR. The thickness was 24, 13, and 7 nm at positions A, B, and C, respectively. As the thickness t of the sample deposited at position B was greater than that of a thin sample (t = 6 nm) deposited at position A, the attainability of TmIG did not depend only on the volume of the film. Rather, it depended also on the chemistry, which is supported by the atomic density of the film evaluated by XRF measurement.

The results of XRF are shown in Fig. 3. The densities of Fe and Tm were evaluated from the XRF spectra using an analysis software equipped with our XRF system (ZSX Primus II, Rigaku) based on Fundamental Parameter (FP) method [18]. Clear peaks are observed from these samples. The ratio of [Tm]/[Fe] was 0.6 (stoichiometric) for the sample fabricated at position A and 0.7 for the other samples (shown in Fig. 2b).

A transportation of ion in material (TRIM) simulation was carried out to clarify the difference in the spreading angles between the sputtered Tm and Fe. The composition versus substrate position is shown with the result of the TRIM simulation in Fig. 4. The kinetic energy of Ar was assumed to be 100 eV or 150 eV, but no significant difference was observed in between these conditions. Sputtered atoms from the target were measured 55 million times. The spreading angles ϕ are counted for each

sputtered atom. Histograms of ϕ of Fe and Tm were made to evaluate the Tm/Fe ratio. The positive trend between ϕ and [Tm]/[Fe] is observed. The density ratio between Tm and Fe is close to 0.6 when the angle ϕ less than 18°. However, in the range of ϕ higher than 20°, the density ratio exceeds 0.7. Hence, it could conceivably be hypothesized that the different sputtering angles between Tm and Fe cause the different chemical compositions of the film in the different positions. A more quantitative understanding of the growth condition dependence of chemical composition will be provided by future research.

The surface morphology of the film displayed in Fig. 5 reveals that the RMS roughness is sufficiently low at 0.4 nm and close to the results reported by other groups[13].

3.2 Perpendicular magnetic anisotropy

Figure 6a displays the hysteresis loop of the TmIG film at position A, which has a thickness of 24 nm. When an applied field is directed in the in-plane direction, the film exhibits a larger saturation field compared to the out-of-plane direction. The observed pattern indicates that the easy axis of the film aligns with the out-of-plane direction, suggesting that the film exhibited PMA properties. The thickness dependence of our film grown at position A is shown in Fig. 6b. The saturation magnetization M_s of the sample thickness of 18, 24, 30 nm are 98, 108, and 55 kA/m, respectively. The decrease of M_s at t = 30 nm is also reported in previous research by Duong *et al* [19], which is attributable to the stress relaxation.

The magnetometry of the samples of different composition is shown in Fig. 6c. All the samples show the hysteresis in *M-H* curves under out-of-plane magnetic field. The magnitude of M_s in growth position of B and C are 23 kA/m and 30 kA/m, which are significantly smaller than that of position A. This decrease in M_s in Tm-rich films is consistent with those of Wu's [14]. They explained the decrease was the result of the Fe vacancies on the tetrahedral sites. Because

of this, in our slightly off-stoichiometric TmIG films the Fe vacancies on the tetrahedral sites reduces magnetic moments.

The effective anisotropy energy K_{eff} was evaluated. FMR-measurements were carried out using the TmIG sample (t = 24 nm) deposited at on-axis position A. An AC field h_{rf} was applied to the sample under a static external field H from different angles relative to the film plane θ_H as shown in Fig. 7a. Figure 7b shows a representative FMR spectrum at $\theta_H = 0^\circ$. Clear FMR signals were observed. The θ_H dependence of the resonance field, H was obtained using the peak search function of commercially available software after integrating the raw data. The angulare dependence is shown in Fig. 7c. The black symbols represent the resonance field $\mu_0 H_{FMR}$. The uniaxial magnetic anisotropy field h_u was evaluated using following equation [20]:

$$\left(\frac{\omega}{\gamma}\right)^2 = [\mu_0 H_{FMR}\cos(\theta_H - \theta) - h_u \cos(2\theta)] \times [\mu_0 H_{FMR}\sin(\theta_H - \theta) + h_u \sin^2 2\theta] = 0 \quad (1),$$

$$\mu_0 H_{FMR}\sin(\theta_H - \theta) + \frac{h_u}{2}\sin 2\theta = 0 \quad (2),$$

where $\omega = 2\pi f$ and $\mu_0 H_{FMR}$ are the angular frequency of the applied microwave and the resonance field obtained from the FMR signal, respectively. θ_H and θ are the angles of the applied magnetic field and saturation magnetization with respect to the film plane, respectively. The lowest value detected at 100° supports that the sample possesses PMA. Equations (1) and (2) were solved self-consistently by substituting in the measured resonance field, and h_u of the TmIG sample was evaluated as -0.16 T. The corresponding $K_{eff} = h_u M_S/2$ was then estimated to be 8.6 kJ/m^3 by considering M_S = 108 kA/m measured by the SQUID in an out-of-plane field. These values are consistent with those reported by other groups using PLD and off-axis sputtering techniques [13,14,19]. The results show that the oxygen ion bombardment of a substrate does not appreciably diminish the magnetic anisotropy or magnetic moment in a magnetic insulator, although in the case of semiconducting devices, it reduces the conductivity of the film [21].

3.3 Analysis and characterization of magnetic domain wall energy

The domain morphology was evaluated by examining samples of various thickness with a polar magneto-optical Kerr effect microscope. Initially, an out-of-plane magnetic field was applied. After AC demagnetization, the microscope image was captured as shown in Fig. 8. A maze domain pattern, which also supports the appearance of PMA, was observed. In addition, we confirmed the maze domain patterns for samples deposited with different thicknesses at position A. All of these results support our main claim of the demonstration of the *on-axis* sputtering fabrication of TmIG with PMA.

Two-dimensional fast Fourier transforms were processed, and the radial averaging of the intensity was computed. The relation between the normalized intensity and radius is shown in Fig. 8d. The stripe spacing D_S, which was evaluated by fitting a Gaussian function, were 28, 11, and 8 μm for thickness 18, 24, 30 nm, respectively.

On the basis of these results, we applied the Kaplan-Gehring model and estimated the energy density of the domain wall σ_{DW}, which is expressed as [12]:

$$\sigma_{DW} = \frac{2K_d t}{\pi} \ln\left[\frac{D_S}{t \exp\left(\frac{\pi b}{2}+1\right)}\right] \quad (3),$$

where b = -0.666 is a model-dependent constant, t is the film thickness, and $K_d = \mu_0 M_s^2/2$ is the dipolar energy constant. The energy density of domain walls was 0.51 mJ/m^2 for 18 nm, 0.69 mJ/m^2 for 24 nm, and 0.2 mJ/m^2 for 30 nm. The smaller M_s resulted in a smaller domain wall energy density (Fig. 8), leading to the smaller domain spacing.These values are on the same order as those for other TmIG films manufactured by PLD or off-axis sputtering [12-14]. The exchange stiffness of the 24 nm thick was evaluated as A_{ex} = 3.4 pJ/m using the relation $A_{ex} = \sigma_{DW}^2/16K_{eff}$. The origin of the difference of A_{ex} might be attributable to the non-uniformity of t of the sample, which had a root-mean-square roughness of 0.4 nm.

4. Conclusions

In summary, we demonstrated the on-axis sputtering deposition of PMA-TmIG. Stoichiometric TmIG was obtained from the sample deposited on a suitable position of the substrate relative to the target. The perpendicular magnetic anisotropy was confirmed by the hysteresis loop patterns, the angle dependence of FMR, a polar magneto-optical Kerr effect microscope. The effective anisotropy was 8.6 kJ/m^3, which is in line with the results of previous studies using PLD and off-axis sputtering [12-14]. Our results show the inertness of magnetic anisotropy and the magnetic moment in the ferrimagnetic insulator to the ion bombardment during deposition. This study showed the possibility of the industrial-friendly production of integrated spintronic devices based on TmIG with PMA.

ACKNOWLEDGMENTS

The authors acknowledge support from JSPS KAKENHI in the form of an Early-Career Scientists grant (No. 22K14292), and Grant-in-Aid for Scientific Research (A) (No. 20H00142), the Iketani Science and Technology Foundation, the Yazaki Memorial Foundation for Science and Technology, and Japan International Cooperation Agency. The authors are grateful to Mr. Kizuku Ikeda for discussions on the analysis of the TRIM simulation. The authors thank Edanz (https://jp.edanz.com/ac) for editing a draft of this manuscript.

REFERENCE

[1] Y. Kajiwara, K. Harii, S. Takahashi, J. Ohe, K. Uchida, M. Mizuguchi, H. Umezawa, H. Kawai, K. Ando, K. Takanashi, S. Maekawa, E. Saitoh, Transmission of electrical signals by spin-wave

interconversion in a magnetic insulator., Nature. 464 (2010) 262–266. https://doi.org/10.1038/nature08876.

[2] H. Nakayama, M. Althammer, Y.T. Chen, K. Uchida, Y. Kajiwara, D. Kikuchi, T. Ohtani, S. Geprägs, M. Opel, S. Takahashi, R. Gross, G.E.W. Bauer, S.T.B. Goennenwein, E. Saitoh, Spin Hall magnetoresistance induced by a nonequilibrium proximity effect, Phys. Rev. Lett. 110 (2013) 206601. https://doi.org/10.1103/PhysRevLett.110.206601.

[3] C.O. Avci, A. Quindeau, C.F. Pai, M. Mann, L. Caretta, A.S. Tang, M.C. Onbasli, C.A. Ross, G.S.D. Beach, Current-induced switching in a magnetic insulator, Nat. Mater. 16 (2017) 309–314. https://doi.org/10.1038/nmat4812.

[4] H. Bai, Z.Z. Zhu, J.T. Ke, G. Li, J. Su, Y. Zhang, T. Zhu, J.W. Cai, Large tunable perpendicular magnetic anisotropy in $Y_{3-x}Tm_xFe_5O_{12}$ (x = 0-3) epitaxial films with minor changes in switching current, Phys. Rev. Appl. 17 (2022) 064023. https://doi.org/10.1103/PhysRevApplied.17.064023.

[5] J. Zou, S. Bosco, B. Pal, S.S.P. Parkin, J. Klinovaja, D. Loss, Quantum computing on magnetic racetracks with flying domain wall qubits, Phys. Rev. Res. 5 (2023) 033166. http://doi.org./10.1103/PhysRevResearch.5.033166.

[6] C. Hauser, T. Richter, N. Homonnay, C. Eisenschmidt, M. Qaid, H. Deniz, D. Hesse, M. Sawicki, S.G. Ebbinghaus, G. Schmidt, Yttrium iron garnet thin films with very low damping obtained by recrystallization of amorphous material, Sci. Rep. 6 (2016) 20827. https://doi.org/10.1038/srep20827.

[7] M. Kubota, A. Tsukazaki, F. Kagawa, K. Shibuya, Y. Tokunaga, M. Kawasaki, Y. Tokura, Stress-induced perpendicular magnetization in epitaxial iron garnet thin films, Appl. Phys. Express. 5 (2012) 103002. https://doi.org/10.1143/APEX.5.103002.

[8] C.O. Avci, E. Rosenberg, M. Baumgartner, L. Beran, A. Quindeau, P. Gambardella, C.A. Ross, G.S.D. Beach, Fast switching and signature of efficient domain wall motion driven by spin-orbit

torques in a perpendicular anisotropy magnetic insulator/Pt bilayer, Appl. Phys. Lett. 111 (2017) 072406. https://doi.org/10.1063/1.4994050.

[9] J.J. Bauer, E.R. Rosenberg, S. Kundu, K.A. Mkhoyan, P. Quarterman, A.J. Grutter, B.J. Kirby, J.A. Borchers, C.A. Ross, Dysprosium iron garnet thin films with perpendicular magnetic anisotropy on silicon, Adv. Electron. Mater. 6 (2020) 1900820. https://doi.org/10.1002/aelm.201900820.

[10] Q. Shao, Y. Liu, G. Yu, S.K. Kim, X. Che, C. Tang, Q.L. He, Y. Tserkovnyak, J. Shi, K.L. Wang, Topological Hall effect at above room temperature in heterostructures composed of a magnetic insulator and a heavy metal, Nat. Electron. 2 (2019) 182–186. https://doi.org/10.1038/s41928-019-0246-x.

[11] S. Vélez, S. Ruiz-Gómez, J. Schaab, E. Gradauskaite, M.S. Wörnle, P. Welter, B.J. Jacot, C.L. Degen, M. Trassin, M. Fiebig, P. Gambardella, Current-driven dynamics and ratchet effect of skyrmion bubbles in a ferrimagnetic insulator, Nat. Nanotechnol. 17 (2022) 834–841. https://doi.org/10.1038/s41565-022-01144-x.

[12] E.R. Rosenberg, K. Litzius, J.M. Shaw, G.A. Riley, G.S.D. Beach, H.T. Nembach, C.A. Ross, Magnetic properties and growth-induced anisotropy in yttrium thulium iron garnet thin films, Adv. Electron. Mater. 7 (2021) 2100452. https://doi.org/10.1002/aelm.202100452.

[13] C.N. Wu, C.C. Tseng, K.Y. Lin, C.K. Cheng, S.L. Yeh, Y.T. Fanchiang, M. Hong, J. Kwo, High-quality single-crystal thulium iron garnet films with perpendicular magnetic anisotropy by off-axis sputtering, AIP Adv. 8 (2018) 055904. https://doi.org/10.1063/1.5006673.

[14] C.N. Wu, C.C. Tseng, Y.T. Fanchiang, C.K. Cheng, K.Y. Lin, S.L. Yeh, S.R. Yang, C.T. Wu, T. Liu, M. Wu, M. Hong, J. Kwo, High-quality thulium iron garnet films with tunable perpendicular magnetic anisotropy by off-axis sputtering – correlation between magnetic properties and film strain, Sci. Rep. 8 (2018) 11087. https://doi.org/10.1038/s41598-018-29493-5.

[15] O. Ciubotariu, A. Semisalova, K. Lenz, M. Albrecht, Strain-induced perpendicular magnetic anisotropy and Gilbert damping of $Tm_3Fe_5O_{12}$ thin films, Sci. Rep. 9 (2019) 17474. https://doi.org/10.1038/s41598-019-53255-6.

[16] U. Betz, M. Kharrazi Olsson, J. Marthy, M.F. Escolá, F. Atamny, Thin films engineering of indium tin oxide: Large area flat panel displays application, Surf. Coatings Technol. 200 (2006) 5751–5759. https://doi.org/10.1016/j.surfcoat.2005.08.144.

[17] K. Alshammari, E. Haltz, M. Alyami, M. Ali, P.S. Keatley, C.H. Marrows, J. Barker, T.A. Moore, Scaling of Dzyaloshinskii-Moriya interaction with magnetization in Pt/Co(Fe)B/Ir multilayers, Phys. Rev. B. 104 (2021) 224402. https://doi.org/10.1103/PhysRevB.104.224402.

[18] T. Shiraiwa, N. Fujino, Theoretical Calculation of Fluorescent X-Ray Intensities in Fluorescent X-Ray Spectrochemical, Jpn. J. Appl. Phys. 5 (1966) 886. https://iopscience.iop.org/article/10.1143/JJAP.5.886.

[19] V.D. Duong, P. Cao Van, T. Nguyen Thi, H.Y. Ahn, V.A. Cao, J. Nah, G. Kim, K.S. Lee, J.W. Kim, J.R. Jeong, Interfacial roughness driven manipulation of magnetic anisotropy and coercivity in ultrathin thulium iron garnet films, J. Alloys Compd. 927 (2022) 166800. https://doi.org/10.1016/j.jallcom.2022.166800.

[20] S. Yoshii, K. Kato, E. Shigematsu, R. Ohshima, Y. Ando, K. Usami, M. Shiraishi, Significant suppression of two-magnon scattering in ultrathin Co by controlling the surface magnetic anisotropy at the Co/nonmagnet interfaces, Phys. Rev. B. 106 (2022) 174414. https://doi.org/10.1103/PhysRevB.106.174414.

[21] A. Bikowski, T. Welzel, K. Ellmer, The impact of negative oxygen ion bombardment on electronic and structural properties of magnetron sputtered ZnO:Al films, Appl. Phys. Lett. 102 (2013) 242106. https://doi.org/10.1063/1.4811647.

FIGURE CAPTIONS

Figure 1: The layout of the substrate holder and target

(a) Schematic side view of the sputtering chamber.

(b) Schematic top view of the substrate holder. The blue cross is the intersection mark between the substrate holder and the normal target. The positions of the substrates are indicated by the pink squares.

Figure 2: XRD patterns

(a) XRD patterns of TmIG films deposited at position A with different of deposition times (150, 90, 30 min) and a bare substrate from top to bottom. The thickness of each film was 30 nm, 18 nm, and 6 nm, respectively.

(b) XRD patterns of TmIG films at positions A, B, C, and substrate from top to bottom.

Figure 3: XRF spectra of TmIG films at position A (red), B (blue), and C (green). (a) Fe and (b) Tm peaks are clearly observed.

Figure 4: TRIM simulation of the dependence of Tm/Fe ratio on angle. (a) Image of the model. Ar ions have the energy of E_{Ar} in x direction and incident on a $Tm_3Fe_5O_{12}$ target. The spreading angles of the sputtered Tm and Fe based on the x axis (ϕ) were measured. The histogram of the spreading angles of Tm and Fe are obtained and the Tm/Fe ratio at each ϕ was calculated. (b) Comparison of the ϕ -dependence of the Tm/Fe ratio. The filled circle and the open triangle represent the results of simulations at E_{Ar} of 100 eV and 150 eV, respectively. The red inverted triangles and the experimental results based on XRF measurement.

Figure 5: The surface morphology in a 2 μm x 2 μm scan area for position A with a thickness 24 nm.

Figure 6: Hysteresis loop of TmIG film measured by SQUID MPMS3. The paramagnetic background of the substrate has been subtracted. (a) Out of plane and in plane field applied at 24

nm. (b) Different thickness. The brown, the red, and the gold plots represent the results of the film thickness of the 18 nm, 24 nm, and 30 nm, respectively. (c) Different position at A, B, and C. Red, blue, and green plots represent the results of the film growth position of A, B, and C, respectively.

Figure 7: Angle dependence of the resonance field

(a) Schematic of the experimental set up. The symbols are defined in the main text.

(b) Representative FMR spectra at $\theta = 0^{\circ}$. The dashed line indicates the value of $\mu_0 H_{FMR}$ (=468 mT).

(c) Angle dependence of $\mu_0 H_{FMR}$. Black symbols and red lines represent experimental results and values using a self-consistent method [20].

Figure 8: Observation of the domain space with different thickness by a Kerr microscope.

(a) 18 nm

(b) 24 nm

(c) 30 nm

(d) Radially averaged intensity of the microscopic image after two-dimensional FFT. The brown, the red, and the gold plots represent the results of the film thickness of the 18 nm, 24 nm, and 30 nm, respectively.

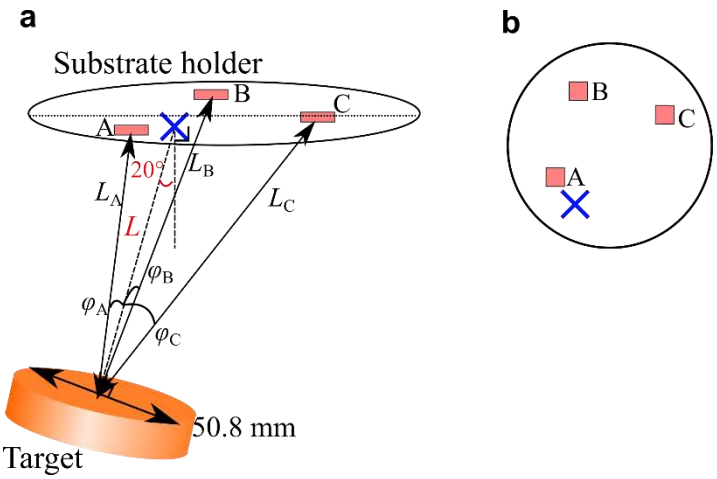

Figure 1. Marlis Nurut Agusutrisno *et al*.

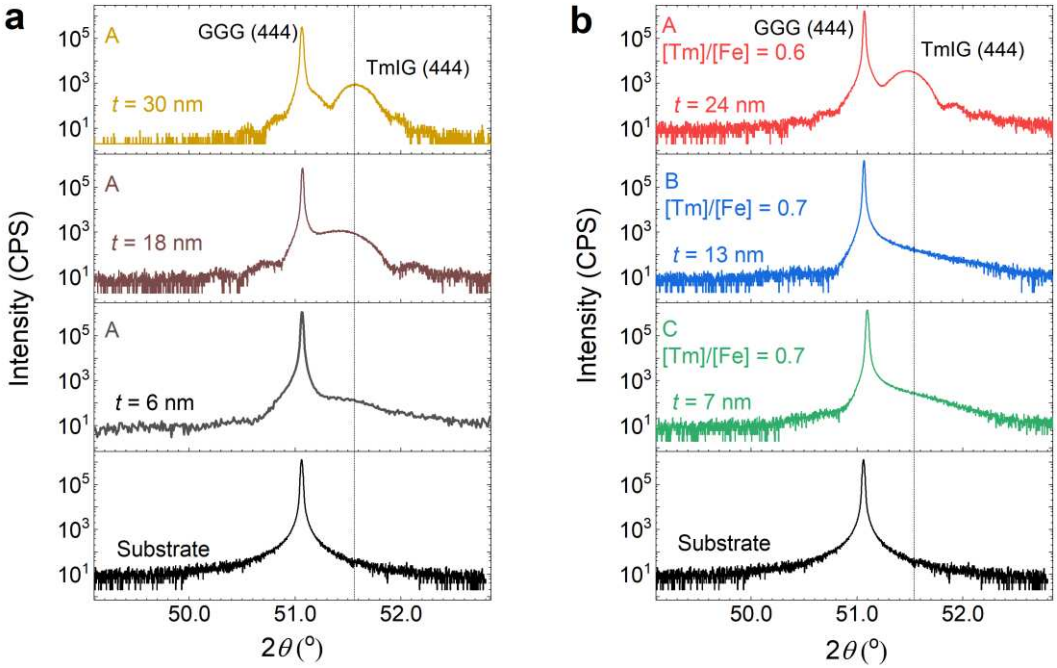

Figure 2. Marlis Nurut Agusutrisno *et al*.

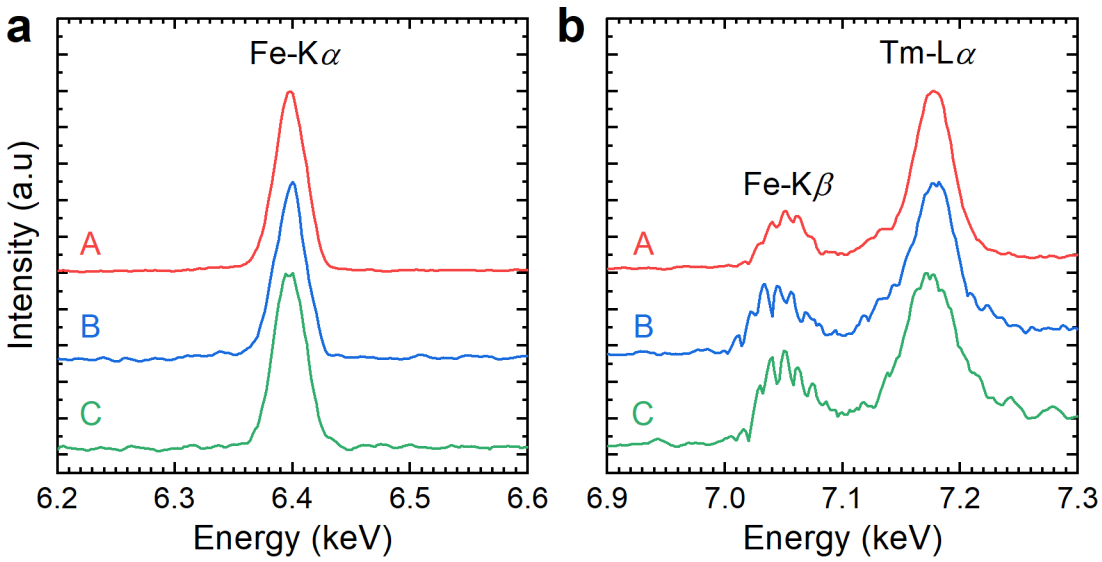

Figure 3. Marlis Nurut Agusutrisno et al.

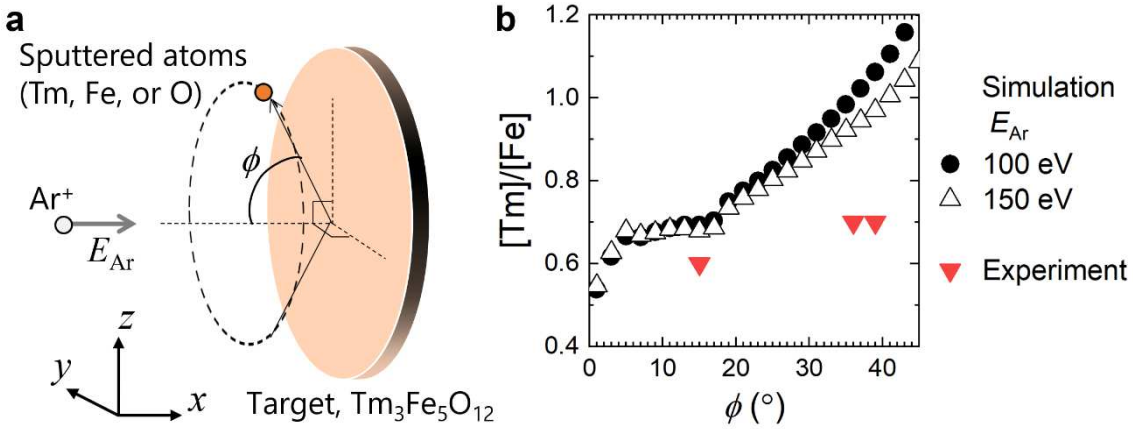

Figure 4. Marlis Nurut Agusutrisno et al.

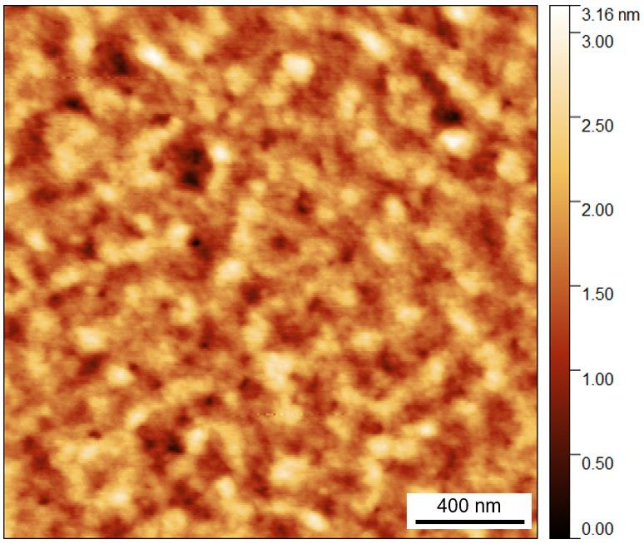

Figure 5. Marlis Nurut Agusutrisno et al.

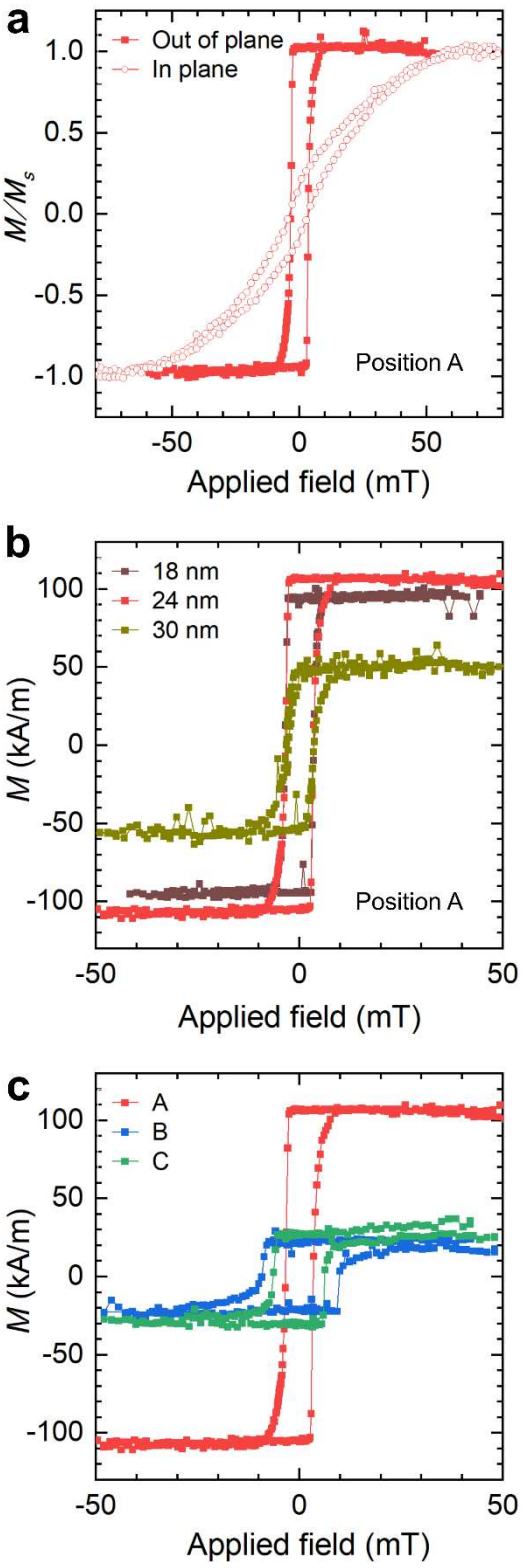

Figure 6. Marlis Nurut Agusutrisno *et al*.

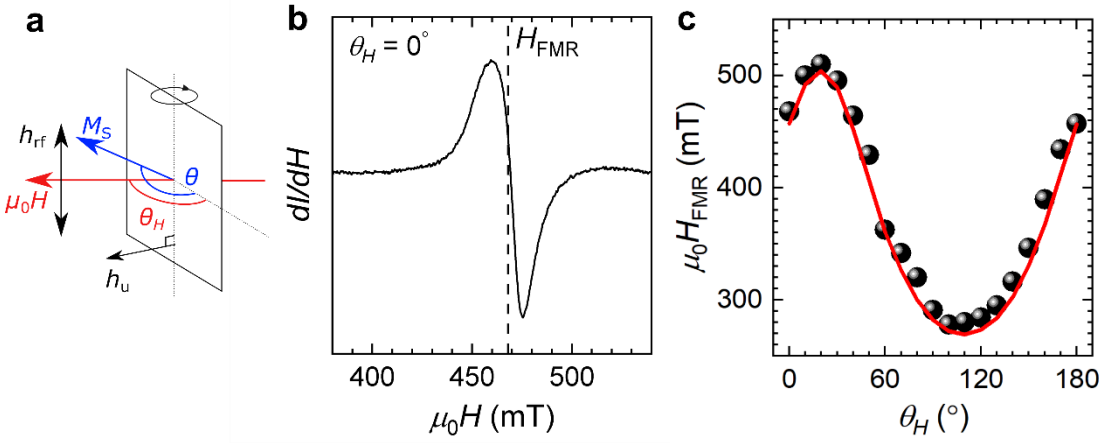

Figure 7. Marlis Nurut Agusutrisno *et al*.

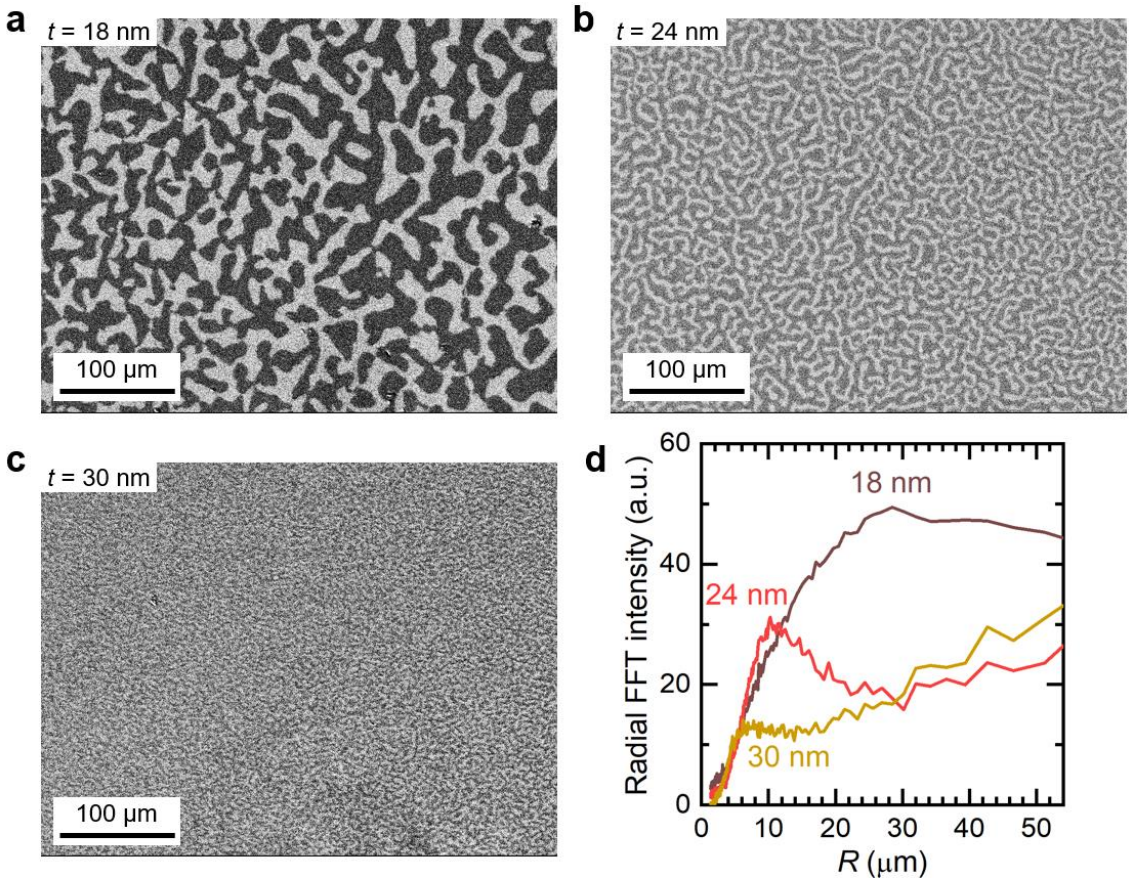

Figure 8. Marlis Nurut Agusutrisno *et al*.